Journal of Luminescence 213 (2019) 427–432

Contents lists available at ScienceDirect

Journal of Luminescence

journal homepage: www.elsevier.com/locate/jlumin

Structural and excitation dependent emission properties of octahedral $CeO_2:Er^{3+}$ nanocrystal

Y. Yang[a,b,c], Y. Cong[c,*], D.P. Dong[c], Y. Xiao[a,b], J.Y. Shang[c], Y. Tong[c], H.M. Zhang[c], M. He[d,**], J.H. Zhang[a,***]

[a] State Key Laboratory of Luminescence and Applications, Changchun Institute of Optics, Fine Mechanics and Physics, Chinese Academy of Sciences, 3888, Eastern South Lake Road, Changchun, 130033, China
[b] University of Chinese Academy of Sciences, Beijing, 100049, China
[c] School of Physics&Materials Engineering, Dalian Nationalities University, Dalian, 11660, China
[d] Department of Physics, College of Science, Dalian Jiaotong University, Dalian, 116028, China

ARTICLE INFO

Keywords:
Luminescence
$CeO_2:Er^{3+}$
Nanocrystals
Li^+ codoping

ABSTRACT

Octahedral $CeO_2:Er^{3+}$ nanocrystals were successfully prepared using a simple hydrothermal method, and the structural and excitation dependent emission properties were investigated in detail. Green ($^2H_{11/2}$, $^4S_{3/2} \rightarrow {}^4I_{15/2}$), red ($^4F_{9/2} \rightarrow {}^4I_{15/2}$) and NIR ($^4I_{11/2} \rightarrow {}^4I_{15/2}$ and $^4I_{13/2} \rightarrow {}^4I_{15/2}$) emission were observed under 980 nm laser diode excitation. The optimal Er^{3+} doping concentration was 3 mol%, and the effect of Li^+ co-dopants with concentration up to 10 mol% on microstructure and emission was investigated. However, for the samples excited under 352 nm down-conversion excitation, the Vis-NIR spectral distribution induced distinct changes related to the excitation mode. Remarkably high enhancement of 1532 nm NIR emission about 12 times was achieved by codoping with Li^+ ions, which make $CeO_2:Er^{3+},Li^+$ nanocrystal a promising candidate for optical amplifier using broadband UV pumping. The possible mechanism of above up-and down-conversion emission and energy transfer process has also been discussed.

1. Introduction

Nanostructured CeO_2-based materials have been used in various research areas in optical coating, oxygen conductor, sensor, catalyst and abrasive materials due to its multifunctional properties such as high refractive index, optical transparency, high dielectric constant, and chemical stability [1–3]. CeO_2 has also gained much attention as a host matrix as well as an activator of phosphor materials because it has a strong absorption of UV light through the charge-transfer (CT) transition from O^{2-} to Ce^{4+} and easily takes part in the energy transfer to other activators [4–6]. Additionally, CeO_2 has low phonon cutoff energy (465 cm^{-1}) and high solubility with rare earth ions. Investigations on rare earth elements, like Er^{3+}, Eu^{3+}, Sm^{3+} and Tb^{3+}, incorporated into CeO_2 nanoparticles have been given much attention in a view of their applications in the fields of bioimaging, optical amplifiers, display devices and UV-LEDs [7,8].

Among them, Er^{3+} ion is the most popular and efficient rare earth ion for optical luminescence and up-conversion because of its characteristics of abundant energy level structure. Er^{3+} exhibits green ($^4S_{3/2} \rightarrow {}^4I_{15/2}$) and red ($^4F_{9/2} \rightarrow {}^4I_{15/2}$) emission bands in the visible region, meanwhile, the near-infrared (NIR) emission around 1540 nm ($^4I_{13/2} \rightarrow {}^4I_{15/2}$) upon 980 nm diode lasers excitation [9]. Therefore, Er^{3+} doped CeO_2 has attracted strong interests due to the spectral application in Vis-NIR region excited by 980 nm laser [10–12]. Since the down-conversion emission studies on Er doped CeO_2 nanoparticles are reported [7], $CeO_2:Er^{3+}$ could be a potential material for harvesting ultraviolet (UV) energy to get Vis-NIR emission. Down- and up-conversion emission studies on Er doped CeO_2 represents a topic of great interest due to the potential applications in theranostics, photonics and bioimaging [7,13–15]. Tiseanu et al. investigated the effect of heterovalent co-dopants on the emission properties of Er–CeO_2 under different excitation conditions [14]. Mu et al. analysed the emission properties of Er–CeO_2 thin film under 340 nm [15]. In these studies, the oxygen vacancies ($V_O^{\cdot\cdot}$) generated by the valence mismatch between the Ln dopant and the Ce host cation are thought to be a key parameter defines the local crystal-field surrounding the Ln with a lower local symmetry

* Corresponding author.
** Corresponding author.
*** Corresponding author.
E-mail addresses: congyan@dlnu.edu.cn (Y. Cong), heming@djtu.edu.cn (M. He), zhangjh@ciomp.ac.cn (J.H. Zhang).

https://doi.org/10.1016/j.jlumin.2019.05.009
Received 18 February 2019; Received in revised form 25 April 2019; Accepted 6 May 2019
Available online 23 May 2019

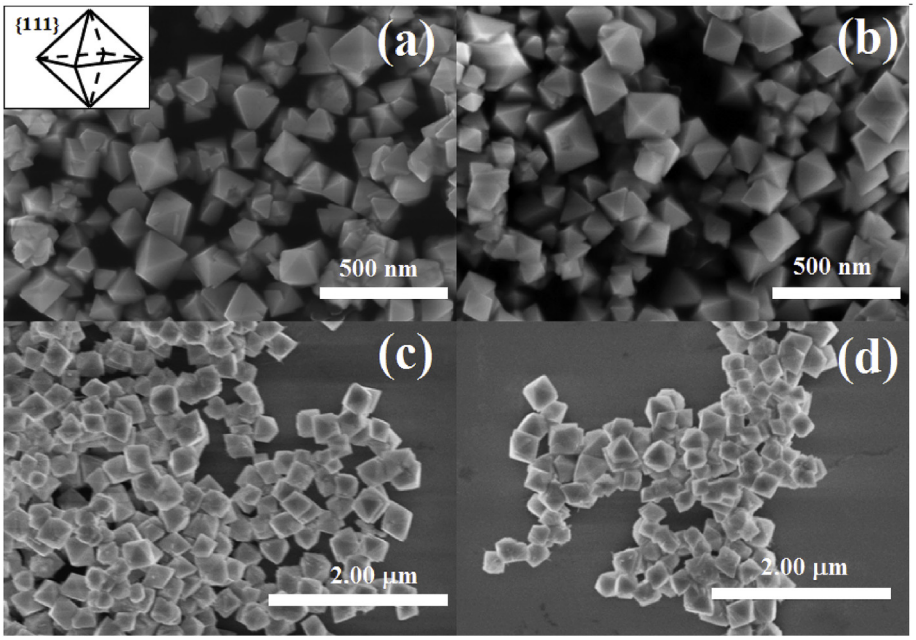

Fig. 1. SEM images of CeO_2: 3 mol% Er^{3+} nanocrystals (a), CeO_2: 3 mol% Er^{3+}, 10 mol% Li^+ (b), and the SEM images of the above nanocrystals with post-calcination temperatures 800 °C (c and d), the inset is a structural model of the octahedral shape.

predicted to induce higher emission intensities. Hence, there is a need of rigorous search for CeO_2: Er^{3+} nanoparticles in order to have the most efficient luminescence properties. In this paper, the luminescence properties including the up-conversion and down-conversion luminescence are investigated, and Li^+ ions are co-doped to improve the NIR emission intensity of CeO_2:Er^{3+} nanocrystals. The energy-transfer mechanism of the excitation dependent emission property is discussed in detail.

2. Experimental

2.1. Synthesis of CeO_2 Er^{3+} and CeO_2: Er^{3+}, Li^+ nanocrystals

CeO_2 nanocrystals were synthesized using a hydrothermal process [16]. The concentration (in mol%) of Er^{3+} and Li^+ are x mol% (x = 1, 3, 5, 7) and y mol% (y = 0, 1, 5, 10) with respect to Ce, respectively. Cerium (III) nitrate hexahydrate ($Ce(NO_3)_3{\cdot}6H_2O$), erbium (III) nitrate pentahydrate ($Er(NO_3)_3{\cdot}5H_2O$), and lithium nitrate ($LiNO_3$) were added to 80 mL of distilled water, and trisodium phosphate dodecahydrate ($Na_3PO_4{\cdot}12H_2O$) was then added to the aqueous solution as a prominent role in the development of the octahedral morphology of the CeO_2 nanocrystals. The mixture was stirred for 1 h, then transferred to a 100 mL teflon-lined stainless steel autoclave and heated at 180 °C for 12 h. Precipitates were collected by centrifugation, washed with water and ethanol, and then dried in an oven. Finally, the obtained powder samples were sintered in air at 800 °C for 3 h.

2.2. Characterization methods

The morphology of the synthesized CeO_2 nanocrystals was observed by scanning electron microscopy (SEM) using Hitachi S-4800. The structural characterization was performed by X-ray diffraction (XRD; Rigaku D/max-IIB) spectra with Cu Kα radiation (λ = 0.15405 nm). Raman spectra were performed with Micro-Raman Spectroscopy System (Renishaw inVia) at laser wavelength of 532 nm. The photoluminescent spectra were measured by an Andor Shamrock SR-750 spectrometer. A charge coupled device (CCD) detector and an InAsGa detector combined with a monochromator were used for signal collection from the UV to NIR region. A continuous 980 nm diode laser was used to pump the samples for the measurement of steady-state emission spectra. In the measurement of down-conversion emission spectra, a tunable Nd:YAG laser pumped OPO laser was used as 352 nm excitation source.

3. Results and discussion

The SEM figures show that the CeO_2 nanocrystals have an octahedral structure with well-defined corners, edges, and mirrorlike facets, corresponding to the (111) plane of CeO_2. The CeO_2 nanoparticles self-assemble to give the well-defined nano-octahedrons with eight (111) planes enclosed with highest surface density of atoms and the lowest surface energy for face-centered cubic structured CeO_2 [16,17]. The octahedral edge lengths range is from 50 to 100 nm, and the particles are well-defined, and some twin and stacking faults between the particles also exists. The agglomeration of nanoparticles is formed during the hydrothermal process, which is due to the existence of mismatch between the lattices, nanoparticles tend to rotate with each other to decrease the interface strain energy. The nanoparticle shape matches very well to the octahedral presented in the inset figure. The Li^+ ions codoping shows less of an effect on the morphology of the CeO_2:Er^{3+} nanoparticles. As shown in Fig. 1b, the particle size and shape of 10 mol % Li^+ codoped sample remain constant, and the nano-octahedrons maintain a smooth, flat surface. After heat treatment at 800 °C for 3 h (see Fig. 1c and d), the octahedral CeO_2 nanoparticles inherit their original morphologies, the size of nano-octahedrons does not change significantly, and the agglomeration is slightly increased.

The crystallinity of the CeO_2:Er^{3+} and Li^+ co-doped CeO_2:Er^{3+} nanocrystals calcined at 800 °C are confirmed by the XRD patterns, and a close inspection of the XRD peaks from 25 to 35° is also given. Since in the eight-fold coordination, the ionic radius of trivalent Er (0.115 nm) is very close to that of Ce^{4+} (0.1098 nm), it is expected that Er^{3+} substitutes for the Ce^{4+} in the crystal lattice. Fig. 2a shows XRD patterns of the CeO_2:Er^{3+} at various Er^{3+} doping concentration, and all the samples crystallize in face-centered cubic fluorite crystal structure (JCPDS 81–0792). No extra peaks are observed in the patterns, indicating that Er^{3+} ions are completely substituted in CeO_2 lattice. However, all diffraction peaks slight shift to lower angle with increasing of Er^{3+} doping concentration which is attributed to the lattice expansion as shown in

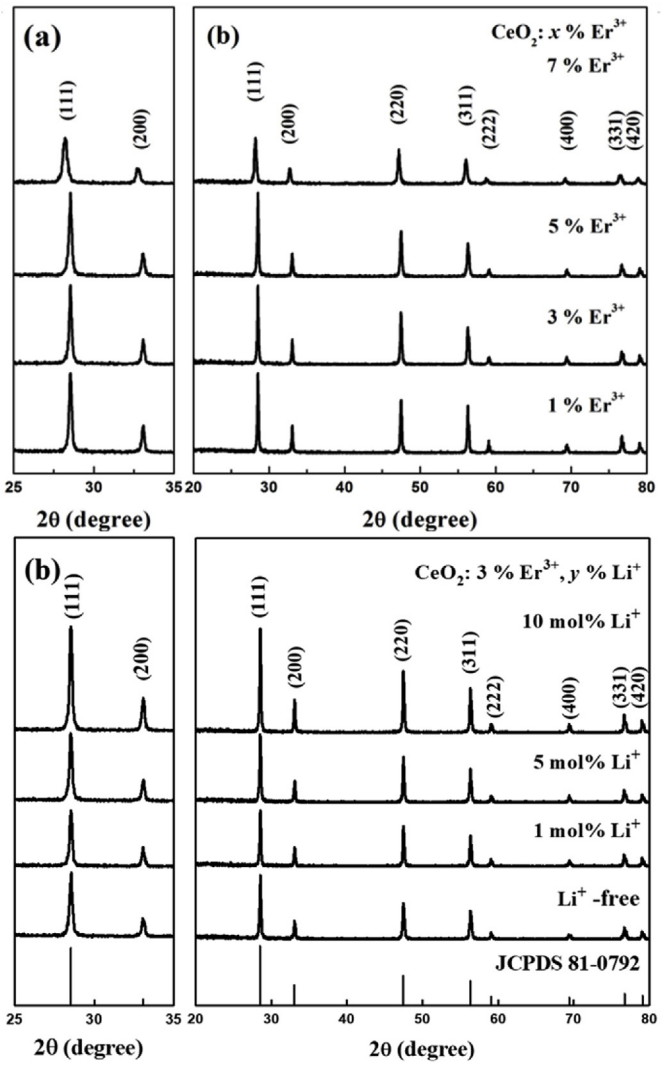

Fig. 2. XRD patterns of CeO_2: x mol% Er^{3+} (x = 1, 3, 5, 7) (a), and CeO_2: 3 mol % Er^{3+}, y mol% Li^+ (y = 0, 1, 5, 10) (b).

Table 1
Lattice constants of Er/Li co-doped CeO_2.

Sample	Lattice constant(Å)
1 mol% Er^{3+}	5.412
3 mol% Er^{3+}	5.413
5 mol% Er^{3+}	5.423
7 mol% Er^{3+}	5.457
co-doped 1 mol% Li^+	5.412
co-doped 5 mol% Li^+	5.412
co-doped 10 mol% Li^+	5.413

the partially enlarged detail of (111) and (200) peaks. A visual comparison is clearly that the 7 mol% Er^{3+} doped sample shows substantially higher peak broadening which could be due to the lattice distortion. The evolution of the lattice constant as a function of Er^{3+} concentration is shown in Table 1. The lattice constant increases with the increasing of Er^{3+} doping concentration, which is in accordance with previous reports [14,18]. The evolution of the lattice gives some indications about the defect distribution inside the grains. The most probable defect formed is the oxygen vacancy ($V_O^{\bullet\bullet}$) on substitution of Er^{3+} for Ce^{4+} due to charge-compensation according to the following reaction equation:

$$Er_2O_3 \xrightarrow{CeO_2} 2Er'_{Ce} + V_O^{\bullet\bullet} + 3O_O^X \quad (1)$$

More defects produced with an increasing concentration of trivalent Er doping, thereby increasing lattice expansion.

Fig. 2b shows XRD patterns of Li^+ co-doped CeO_2:3 mol% Er^{3+}. The CeO_2:3 mol% Er^{3+} sample shows a pure cubic fluorite phase, and the Li^+ codoping do not generate any impurity peaks. The substitution of Ce^{4+} with the smaller Li^+ is expected to generate more oxygen vacancies to compensate for the introduced negative charge of Li'''_{Ce} cations. However, No obvious lattice distortion is induced by the insertion of Li^+ into the ceria lattice, only a slight asymmetry on the smaller angle side is observed for the highest Li concentration. Lattice constant has a slight decrease by co-doping with 1% Li^+, then remain almost same with higher Li^+ doping concentration as shown in Table 1. It is suggested that a very limited Li incorporation and generation of defects in the CeO_2:Er lattice. On the other hand, the crystallinity of CeO_2 is largely improved by the Li^+ ions. According to the previous research, monovalent Li is an efficient promoter of the sintering processes and electrical properties such as gain interior and grain boundary conductivity [19].

The Raman spectra in Fig. 3a show the Er^{3+} doping CeO_2 introduces a significant amount of oxygen vacancies. The Raman spectrum of 1 mol% Er^{3+} doped CeO_2 is dominated by a peak at around 464 cm^{-1}, which is corresponding to the cubic fluorite lattice. The defect band at around 570 cm^{-1} is attributed to oxygen vacancies [14,20]. With the increase of Er^{3+} concentration, the Raman spectra progressively shift to lower energies (from 464 cm^{-1} to 456 cm^{-1}). The shifts indicated a lattice expansion consistently with the XRD results. And the $V_O^{\bullet\bullet}$ band around 570 cm^{-1} is progressively enhanced with Er^{3+} concentration, which proves that the Er^{3+} doping introduces a significant amount of oxygen vacancies. On the other hand, the peak at 464 cm^{-1} of CeO_2:Er remains basically unperturbed by Li co-doping as shown in Fig. 3b. And no excess oxygen vacancies generated from Li co-doping according to the Raman spectra results. The results sustain a very limited Li incorporation within the CeO_2:Er lattice consistently with the XRD results.

Fig. 4 shows Vis-NIR emission spectra of CeO_2:Er^{3+} nanocrystals with different concentrations excited by 980 nm. The visible spectra exhibit two emission bands, a green band at 525/550 nm ($^2H_{11/2}$, $^4S_{3/2} \rightarrow {}^4I_{15/2}$ transitions), and a red band at 654/678 nm ($^4F_{9/2} \rightarrow {}^4I_{15/2}$ transitions). In NIR region, the emission bands centered at 1000 nm ($^4I_{11/2} \rightarrow {}^4I_{15/2}$) and 1500 nm ($^4I_{13/2} \rightarrow {}^4I_{15/2}$) are observed. Moreover, both the visible and NIR emissions show remarkable concentration dependence. Er^{3+}-Er^{3+} energy transfer occurs due to the excessive concentration of Er^{3+} ions, and the optimal Er^{3+} doping concentration to achieve the highest visible emission intensity is 3 mol%. The nonequivalent substitution of Er^{3+} for Ce^{4+} creates an excess oxygen vacancy defects, resulting in enhanced quenching centers in the nanocrystals [21,22]. The probability of non-radiative transition increased due to more Er^{3+} ions transfer energy to nearby quenching centers, the intensity of emissions decreased due to the concentration quenching effect [23].

It is remarkable to see a different quenching concentration in the NIR emission spectra. The visible emission reaches a maximum with 3 mol% Er^{3+} doping concentration and that of NIR emission is more higher, the emission intensity increases with increasing Er^{3+} concentration in the doping range. This can be explained by the cross relaxation (CR) processes described in the energy level diagram of Er^{3+} (see inset in Fig. 4). As Er^{3+} concentration increases, the CR processes become more efficient due to shorter distance between the ions. According to the energy level diagram of Er^{3+}, four CR processes were purposed:

(1) $^4F_{7/2} + {}^4I_{11/2} \rightarrow 2\ {}^4F_{9/2}$
(2) $2\ {}^4I_{11/2} \rightarrow {}^4F_{7/2} + {}^4I_{15/2}$
(3) $^4I_{15/2} + {}^4S_{3/2}/{}^2H_{11/2} \rightarrow {}^4F_{9/2} + {}^4I_{13/2}$

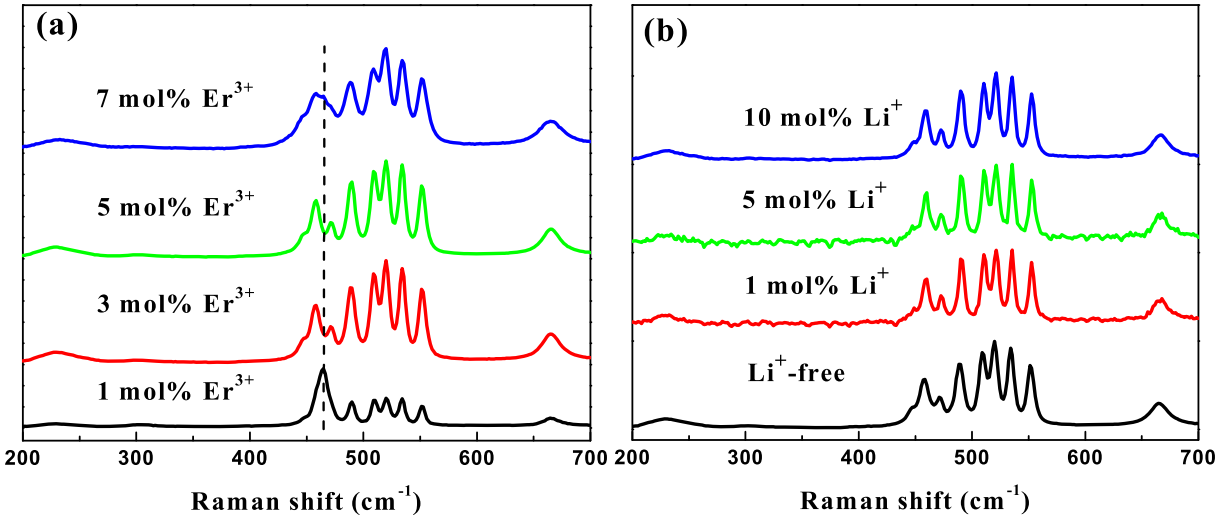

Fig. 3. Effect of Er^{3+} (a) and Li^{+} co-doping (b) on Raman spectra of CeO_2.

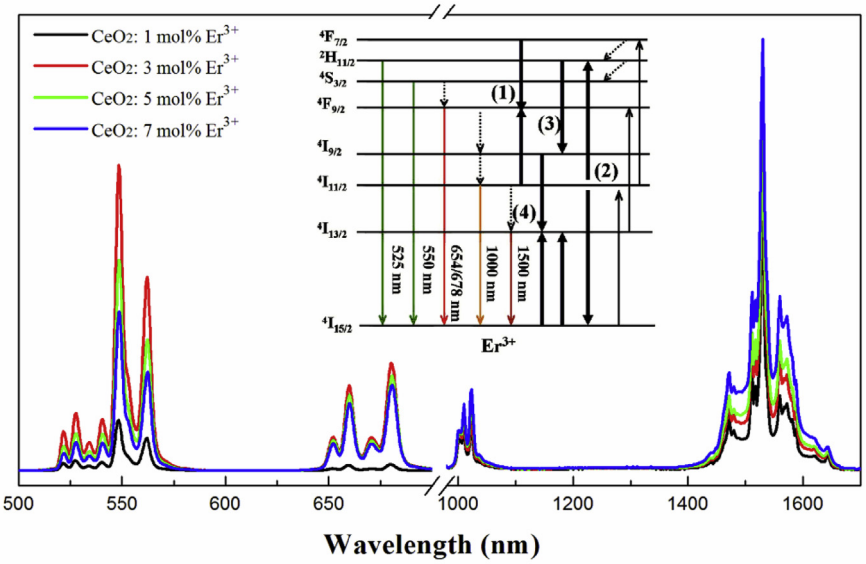

Fig. 4. Visible (left) and NIR (right) emission spectra of CeO_2: x mol% Er^{3+} (x = 1, 3, 5, 7) nanocrystals, the inset shows the energy level diagram of Er^{3+} and the possible CR processes.

(4) $^4I_{15/2} + {}^4I_{9/2} \rightarrow 2\ {}^4I_{13/2}$

The CR1 and CR 2 processes lead to the population of the $^4F_{7/2}$ and $^4F_{9/2}$ leveals, as Er^{3+} concentration increases, the CR processes become more efficient due to shorter distance between the ions. Accordingly, increasing the processes of CR1 and CR2 lead to increased population of the $^4F_{7/2}$ and $^4F_{9/2}$ leveals. The CR3 and CR4 processes result in populating electrons in the $^4I_{13/2}$ levels, and decrease population of the $^4S_{3/2}/^2H_{11/2}$ simultaneously. So the higher concentration contributes to the CR3 and 4 processes, which make a higher quenching concentration in NIR emission. Therefore, the emission properties and the quenching concentration can be mediated by the dopant concentrations.

Visible and NIR emission of Er^{3+} has also been obtained from CeO_2: Er^{3+} nanocrystals under down-conversion excitation into the CeO_2 charge-transfer (CT) band (about 352 nm) excitation, and the emission shape is strongly modulated by the excitation mode. As shown in Fig. 5, the red to green emission ratio (ratio of intensities of $^4F_{9/2} \rightarrow {}^4I_{15/2}$ and $^2H_{11/2}$, $^4S_{3/2} \rightarrow {}^4I_{15/2}$ transitions) is significantly decreased for the samples under CT excitation. In the NIR spectral region, the 1000–1530 nm emission ratio (ratio of intensities of $^4I_{11/2} \rightarrow {}^4I_{15/2}$ and $^4I_{13/2} \rightarrow {}^4I_{15/2}$ transitions) is also significantly decreased. In this case, it is the green emission dominates the visible spectra, and the 1530 nm emission dominates the NIR spectra of CeO_2: Er^{3+} sample. Remarkably, enhancement of the NIR emission as much as 12 times has been achieved by optimal codoping with Li^{+} ions under down-conversion excitation. Compared to CT excited emission, the emission intensity and spectral distribution remain basically unperturbed by Li presence upon 980 nm excitation (Fig. S1).

A simplified diagram illustrating the possible mechanism of down-converted emission and energy transfer process is depicted in Fig. 6. Upon the UV excitation, part of the excited electrons in CeO_2 are relaxed to Er^{3+} ions through the nonradiative energy transfer process, which result in populating electrons in the $^2G_{7/2}$ levels. The electrons then decayed to $^4F_{7/2}$ energy level, the populated $^4F_{7/2}$ may mostly nonradiatively relax to the $^2I_{11/2}$ and $^4S_{3/2}$ levels, which produce green emission of 525/550 nm. Meanwhile, two CR processes occurred: (1) CR energy transfer of ($^4S_{3/2} \rightarrow {}^4I_{9/2}$, $^4I_{15/2} \rightarrow {}^4I_{13/2}$) occurred, after the $^4S_{3/2}$ level was populated; (2) CR energy transfer of ($^4I_{9/2} \rightarrow {}^4I_{13/2}$, $^4I_{15/2} \rightarrow {}^4I_{13/2}$) then consequently occurred [24,25]. Therefore, this two CR processes lead to the population of the $^4I_{13/2}$ level, which greatly

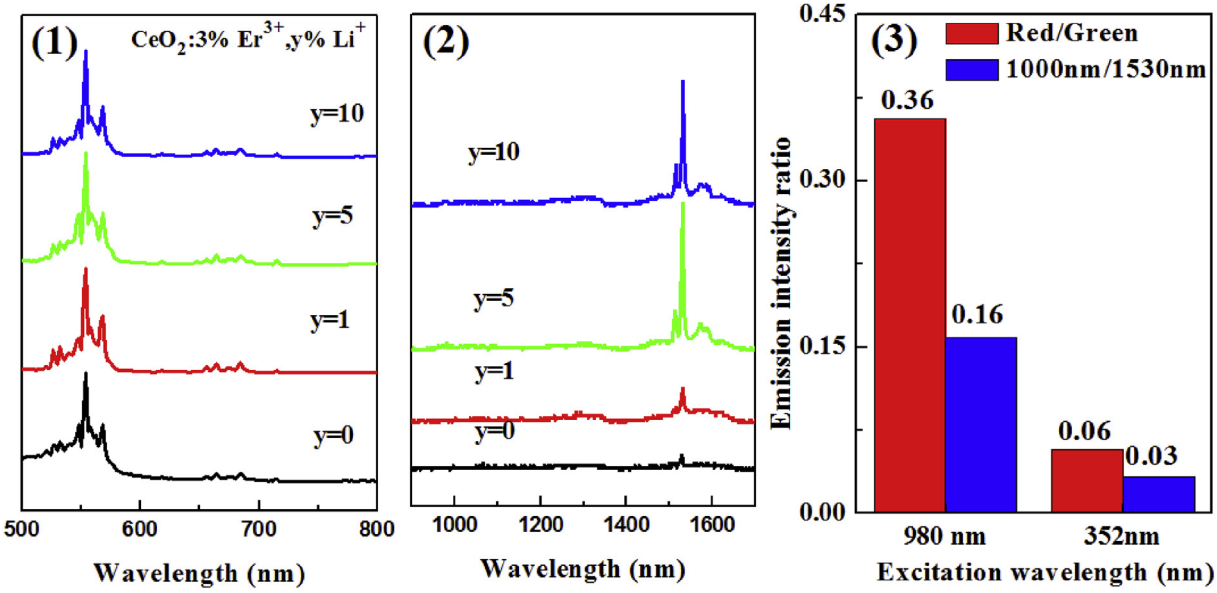

Fig. 5. Visible (1), NIR (2) emission spectra of CeO_2: 3 mol% Er^{3+}, y% Li^+ excited by 352 nm, and the value of I_{red}/I_{green}, and I_{1000nm}/I_{1530nm} under 980 and 352 nm excitation (3).

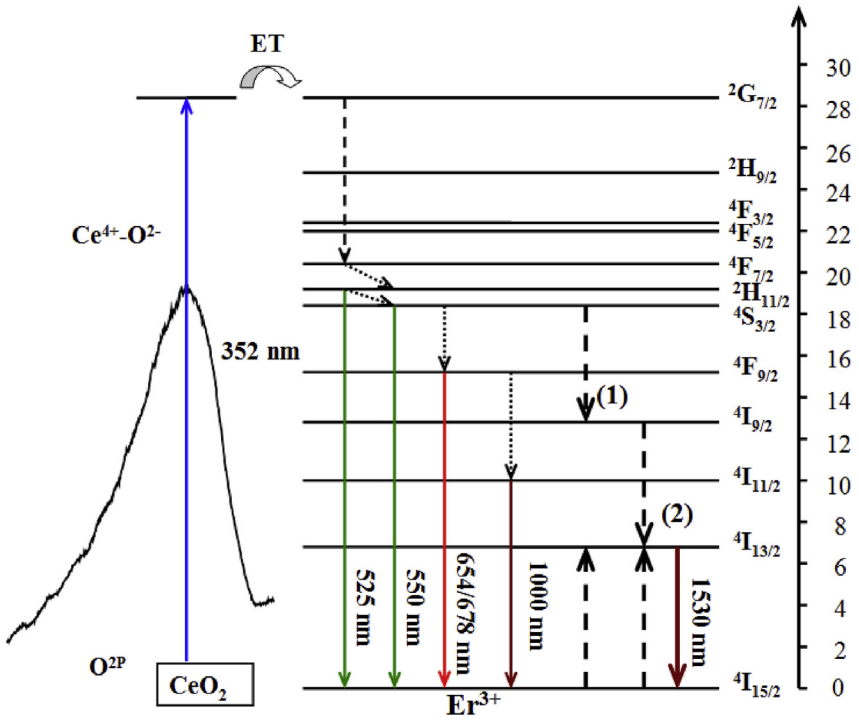

Fig. 6. Schematic energy level diagram of CeO_2:Er^{3+}, Li^+ upon 352 nm excitation.

enhance the 1532 nm NIR emission of the Er^{3+} ions. Meanwhile, the CR process also effected the population of $^4F_{9/2}$ and $^4I_{11/2}$ levels, which explain well the decrease of the 654/678 nm ($^4F_{9/2} \rightarrow {}^4I_{15/2}$ transitions) and 1000 nm ($^4I_{11/2} \rightarrow {}^4I_{15/2}$) emissions.

Li^+ ion is well known for its ability to strongly enhance the emission of a wide range of Li, Lanthanide co-doped materials [26,27]. A series of CeO_2:3 mol% Er^{3+} nanocrystal samples codoping with different concentrations of Li^+ ions are prepared. It is clearly shown in Fig. 5 that the emission intensity of 1532 nm increased dramatically with the Li^+ codoping for about 12 times. Li^+ ions with a small size occupy the interstitial sites in CeO_2:Er^{3+} lattice modify the structure slightly. In addition to improving crystallization (as shown in XRD results), lowering of the local symmetry around Er^{3+} by Li^+ co-doping is an important factor. The lowering symmetry is propitious to 4f radiation transition of rare earth, leading to enhancement of emission intensity of rare earth ions [28,29]. UV excitable NIR emission at 1532 nm may render CeO_2:Er^{3+}, Li^+ nanocrystals attractive for optical amplifier.

4. Conclusions

CeO_2:Er^{3+} nanocrystals were synthesized by a simple hydrothermal method, and luminescence properties and morphology were systematically studied depending on excitation mode. The prepared octahedral CeO_2:Er^{3+} nanophosphor was crystallized in pure cubic fluorite CeO_2.

Vis-NIR emission was observed under optical up-and down-conversion excitation, and the effect Li^+ ions doping was investigated. The emission mechanism and energy transfer process may explain the emission intensity and spectral distribution. For the Li^+ co-doped CeO_2:Er^{3+} samples, the improving crystallization and lowering local symmetry are responsible for the enhancement of the 1532 nm emission intensity under excitation of 352 nm.

Acknowledgments

This work is supported by National Natural Science Foundation of China (Grant nos. 11874101 and 11874055), Program for New Century Excellent Talents in University (Grant no. NCET-13-0702), Science and Technology Project of Liaoning Province (Grant no. 2012222009), Natural Science Foundation of Liaoning Province (Grant nos.20170540200 and 20180550).

Appendix A. Supplementary data

Supplementary data to this article can be found online at https://doi.org/10.1016/j.jlumin.2019.05.009.

References

[1] S. Bahu, J.H. Cho, J.M. Dowding, E. Heckert, C. Komanski, S. Das, J. Colon, C.H. Baker, M. Bass, W.T. Self, S. Seal, Chem. Commun. 46 (2010) 6915.
[2] T. Taniguchi, Y. Sonoda, M. Echikawa, Y. Watanabe, K. Hatakeyama, S. Ida, M. Koinuma, Y. Matsumoto, ACS Appl. Mater. Interfaces 4 (2012) 1010.
[3] J.-X. Feng, S.-H. Ye, H. Xu, Y.-X. Tong, G.-R. Li, Adv. Mater. 28 (2016) 4698.
[4] Y. Sohn, J. Am. Ceram. Soc. 96 (2013) 3747.
[5] C. Sorbello, B.C. Barja, M. Jobbágy, J. Mater. Chem. C 2 (2014) 1010.
[6] B.H. Min, J.C. Lee, K.Y. Jung, D.S. Kim, B.-K. Choi, W.-J. Kang, RSC Adv. 6 (2016) 81203.
[7] X. Yu, P. Xie, Q. Su, Phys. Chem. Chem. Phys. 3 (2001) 5266.
[8] S. Shi, M. Hossu, R. Hall, W. Chen, J. Mater. Chem. 22 (2012) 23461.
[9] B. Dong, B.S. Cao, Y.Y. He, Z. Liu, Z.P. Li, Z.Q. Feng, Adv. Mater. 24 (2012) 1987.
[10] J.H. Cho, M. Bass, S. Babu, J. Dowding, W.T. Self, S. Seak, J. Lumin. 132 (2012) 743.
[11] Y. Guo, D. Wang, F. Wang, Opt. Mater. 42 (2015) 390.
[12] M. Yada, T. Miyaguchi, D. Watanabe, Y. Hayashi, T. Ayabe, T. Torikai, T. Watari, Crys. Eng. Comm. 18 (2016) 8377.
[13] Y. Guo, D. Wang, F. Wang, Opt. Mater. 42 (2015) 390.
[14] M. Florea, D. Avram, B. Cojocaru, I. Tiseanu, V. Parvulescu, C. Tiseanu, Phys. Chem. Chem. Phys. 18 (2016) 18268.
[15] G. Mu, S. Wang, L. Li, X. Yin, G. Wan, Y. Tang, L. Yi, J. Alloy. Comp. 664 (2016) 690.
[16] L. Yan, R. Yu, J. Chen, X. Xing, Cryst. Growth Des. 8 (2008) 1474.
[17] Z. Wang, X. Feng, J. Phys. Chem. B 107 (2003) 13563.
[18] B.M. Reddy, L. Katta, G. Thrimurthulu, Chem. Mater. 22 (2010) 467.
[19] T. Zhu, Y. Lin, Z. Yang, D. Su, S. Ma, M. Han, F. Chen, J. Power Sources 261 (2014) 255.
[20] F. Giannici, G. Gregori, C. Aliotta, A. Longo, J. Maier, A. Martorana, Chem. Mater. 26 (2014) 5994.
[21] D. Avram, M. Sanchez-Dominguez, B. Cojocaru, M. Florea, V. Parvulescu, C. Tiseanu, J. Phys. Chem. C 119 (2015) 16303.
[22] I. Porosnicu, D. Avram, B. Cojocaru, M. Florea, C. Tiseanu, J. Alloy. Comp. 711 (2017) 627.
[23] S. Yang, H. Xia, Y. Jiang, J. Zhang, Y. Shi, X. Gu, J. Zhang, Y. Zhang, H. Jiang, B. Chen, J. Alloy. Comp. 643 (2015) 1.
[24] F. Xiao, R. Chen, Y.Q. Shen, Z.L. Dong, H.H. Wang, Q.Y. Zhang, H.D. Su, J. Phys. Chem. C 116 (2012) 13458.
[25] X.B. Chen, J.G. Wu, X.L. Xu, Y.Z. Zhang, N. Sawanobori, C.L. Zhang, Q.H. Pan, G.J. Salamo, Opt. Lett. 34 (2009) 887.
[26] A.K. Singh, S.K. Singh, S.B. Rai, RSC Adv. 4 (2014) 27039.
[27] B.S. Cao, Z.Q. Feng, Y.Y. He, H. Li, B. Dong, J. Sol. Gel Sci. Technol. 54 (2010) 101.
[28] G.Y. Chen, H.C. Liu, H.J. Liang, G. Somesfalean, Z.G. Zhang, J. Phys. Chem. C 112 (2008) 12030.
[29] X.Q. Gu, L.P. Zhu, Z.Z. Ye, H.P. He, Y.Z. Zhang, B.H. Zhao, Thin Solid Films 517 (2009) 5134.